The effect of surface tension on the stability of unconfined and confined planar jets and wakes

S. J. R E E S AND M. P. J U N I P E R†

Department of Engineering, University of Cambridge, Trumpington Street, Cambridge CB2 1PZ, UK

In this theoretical study, a linear spatio-temporal analysis is performed on unconfined and confined inviscid jet/wake flows with surface tension in order to determine convective/absolute instability criteria. There is a single mode that is due to surface tension and many modes that are due to the jet/wake column. In the unconfined case, the full impulse response is considered in the entire outer flow. On the one hand, the surface tension mode propagates slowly in the cross-stream direction but dominates at the front and back of the wavepacket. On the other hand, the jet/wake column modes propagate more quickly in the cross-stream direction and therefore define the boundaries of the central region of the wavepacket. The flow is particularly unstable when these modes interact. For unconfined flows, it is found that at low and intermediate surface tensions the flow can be more absolutely unstable than that without surface tension but at high surface tensions the flow is stabilized. The effect of confinement has previously been studied but not with the inclusion of surface tension. Confinement and surface tension combined cause the transition from convective to absolute instability to occur even with significant coflow. This effect is examined over an infinite domain of density ratios and confinement.

1. Introduction

This paper describes the combined effect of surface tension and confinement on the stability of incompressible planar jets and wakes. These flows consist of a central sheet of one fluid sandwiched between two identical sheets of another fluid. These sheets are confined between two flat plates, as shown in figure 1, and there is a finite surface tension between the two fluids. In a jet flow, the inner fluid moves faster than the outer fluid. In a wake flow, the outer fluid moves faster than the inner fluid.

Several factors can affect the stability of jets and wakes. The most important are: the shear number Λ, which is based on the bulk velocities in the inner and outer flows and describes the amount of shear and the type of flow (jet or wake, coflow or counterflow); the shear layer velocity profile, which to a great extent can be described by the ratio of the shear layer thickness to the jet/wake width; the density ratio between the inner and the outer flows; the Reynolds number; the confinement parameter h, if the outer flow is confined within a duct, and the Weber number (non-dimensional surface tension) if the inner and outer flows are immiscible.

This paper is one of the series whose aim is to analyse theoretically the effect of each parameter and understand physically how they act and interact. In each paper, only a few parameters are examined simultaneously so that the problems remain

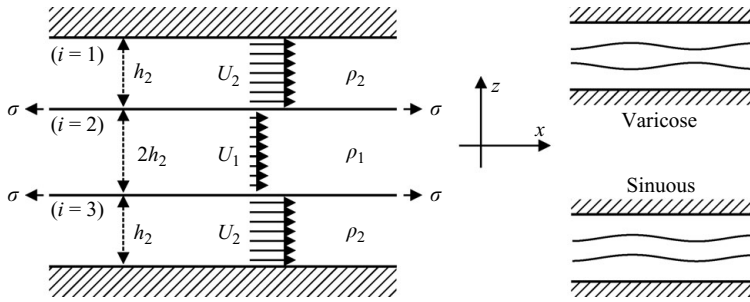† Email address for correspondence: mpj1001@eng.cam.ac.uk

FIGURE 1. The model consists of three flows. When unconfined, the outer flows have infinite extent in the cross-stream direction. When confined, they are sandwiched between two flat plates. Each fluid has a constant density and a uniform velocity. There is a restoring force at the interface due to surface tension.

manageable. Juniper (2006) examines the effect of shear, confinement parameter and density ratio on plug flow planar jets and wakes; Juniper (2007, 2008) include the effect of shear layer thickness on planar and round jets and wakes; in a paper parallel to this one, Rees & Juniper (in press) examine the effect of shear, Reynolds number and shear layer thickness on confined planar jets and wakes. This paper examines shear, non-dimensional surface tension, confinement parameter and density ratio. Surface tension introduces a new length scale into the problem and it is particularly interesting to see how this interacts with the thickness of the inner flow and, when the flow is confined, the thickness of the outer flow.

The shear number is defined as $\Lambda = (U_1 - U_2)/(U_1 + U_2)$, where U_1 is the velocity of the inner flow and U_2 is the velocity of the outer flow. It characterizes the magnitude of the shear and the type of flow. A wake flow corresponds to $\Lambda < 0$ and a jet flow corresponds to $\Lambda > 0$. Coflow corresponds to $|\Lambda| < 1$ and counterflow corresponds to $|\Lambda| > 1$. The shear number has fairly straightforward effects: higher shear corresponds to higher perturbation growth rates and counterflow is more absolutely unstable than coflow (Yu & Monkewitz 1990).

Whether Λ is kept constant or treated as a parameter depends on the type of stability analysis. Conventional stability analyses are performed by examining the response at a point in space to an impulse at the same point in space (i.e. along the ray $x/t = 0$ and $z/t = 0$, where x is the streamwise coordinate and z is the cross-stream coordinate). In such analyses, Λ is a crucial parameter for distinguishing between absolute and convective instabilities. Recent stability analyses, however, have examined the impulse response either along the streamwise coordinate (i.e. for general x/t at $z/t = 0$) or along both the streamwise and cross-stream coordinates simultaneously (i.e. for general x/t and z/t). Examples of the streamwise impulse response can be found in Lesshafft & Huerre (2007) for hot round jets and Meliga, Sipp & Chomaz (2008) for round wakes. Examples of the full impulse response can be found in Healey (2007) for the rotating disk boundary layer, Juniper (2007) for planar jets and wakes and Juniper (2008) for round jets and wakes. The impulse response is calculated at one value of Λ and then absolute/convective instability is inferred at other values of Λ by examining the response along rays $x/t \neq 0$. In summary, in the conventional analyses, one value of x/t is chosen and Λ is a parameter in the problem, while in the full impulse response analyses, one value of Λ is chosen and x/t is a parameter in the problem. In this paper, the conventional analysis is used to map out regions of absolute instability in parameter space and the full impulse

response analysis is used to explain the effects physically in terms of the interaction between surface tension and jet/wake column modes.

In a single shear layer, the velocity profile can be described to a great extent just by the shear layer thickness δ, which gives the cutoff wavelength below which perturbations are stabilized. The exact shape of its velocity profile does not qualitatively change its stability characteristics, whether viscous or inviscid (Esch 1957). In a temporal stability analysis, for instance, this shape merely fine-tunes the cutoff wavelength.

The same is true for double shear layers. Jet/wake velocity profiles are characterized by two parallel shear layers of equal and opposite vorticity. In a spatio-temporal stability analysis, there is a single saddle point caused by the individual shear layers (called 'mode I' in Jendoubi & Strykowski 1994, 's_1' in Juniper 2007 and 'shear layer mode' in Lesshafft & Huerre 2007). There are also an infinite number of saddle points caused by the interaction between the two shear layers (called 'mode II' in Jendoubi & Strykowski 1994, 's_2' in Juniper 2007 and 'jet column modes' in Lesshafft & Huerre 2007). The ratio of the shear layer thickness δ, to the shear layer half-spacing h_1, is a particularly important parameter because, in the wavenumber plane, the s_1 saddle sits near the k_r-axis at $k_r \sim 1/\delta$ and the s_2 saddle points sit near the k_i-axis at $k_r \sim 1/h_1$. As this ratio decreases, the distance between the s_1 and s_2 saddle points increases. When the s_1 saddle point is distant from the s_2 saddle points, the exact velocity profile in each shear layer has no effect on the s_2 saddle points. Physically, this is because the jet/wake column mode has a long wavelength, whose eigenfunction extends far outside the shear layers and does not 'see' the exact velocity profile in each shear layer (Yu & Monkewitz 1990). In conclusion, the exact velocity profile in the shear layers does not qualitatively change a jet/wake flow's stability characteristics.

The density ratio between the inner and the outer flows has a strong effect on the instability of jets and wakes, particularly on the transition between convective and absolute instabilities. In a theoretical study on planar flows, Yu & Monkewitz (1990) showed that high-density wakes and low-density jets are particularly absolutely unstable. In experimental studies on low-density jets, the same result was found for round jets (Sreenivasan, Raghu & Kyle 1989) and planar jets (Yu & Monkewitz 1993). For a single shear layer with finite thickness, the full impulse response centres around the ray with velocity $x/t = (\rho_1 U_1 + \rho_2 U_2)/(\rho_1 + \rho_2)$ and therefore tends towards the velocity of the denser fluid. This explains why high-density wakes and low-density jets are particularly absolutely unstable: strong shear is generated by the light fluid, which is fast, but the speed of the centre of the wavepacket is given by the dense fluid, which is slow. More recently, Lesshafft & Huerre (2007) have shown that this arises through the action of baroclinic torque. If this is removed via a body force then the low-density jet, for instance, recovers the instability characteristics of a uniform density jet.

Confining jets or wakes within a duct significantly alter their stability, and this effect depends on the Reynolds number. The inviscid case has been examined theoretically by Juniper (2006) for planar jets and wakes and by Juniper (2008) for round jets and wakes. In these studies, the confinement parameter h, is defined as the width of the outer fluid divided by the half-width of the inner fluid. These studies show that confinement destabilizes uniform density wake flows around $h \sim 1$ and uniform density jet flows around $h \sim 2$. The destabilizing effect is even stronger when confinement is combined with a density ratio. This is exploited in the fuel injectors of rocket engines, which are confined dense wakes, to create good mixing between the two reactants (Juniper & Candel 2003).

At low Reynolds number in unconfined shear flows, viscosity has a stabilizing effect. This is shown by Esch (1957) for a single shear layer at $Re \leqslant 1000$ and by Monkewitz (1988) and Yu & Monkewitz (1990) for unconfined wakes at $Re \leqslant 100$. It would be useful to know the Reynolds number above which viscosity can be neglected. From the single shear layer results of Esch (1957), this is around $Re = 200$. For the wake flows of Monkewitz (1988) and Yu & Monkewitz (1990), the maximum Reynolds number studied was $Re = 100$ and, although the results were close to the inviscid results, they could not be said to be identical. For higher Reynolds numbers it is necessary to look elsewhere. The studies most relevant to this paper, presented below, are for confined viscous wakes.

At high Reynolds number, confinement destabilizes jets and wakes. As well as the theoretical studies already mentioned, this is seen particularly clearly in the experimental study of Richter & Naudascher (1976), who examined the fluctuating forces on a confined circular cylinder at $10^4 < Re < 10^6$. The fluctuating cross-stream force, which arises from sinuous vortex shedding, increased markedly as the flow was confined, becoming eight times greater than the unconfined case when the cylinder's diameter was half the distance between the plates ($h = 1$, $\beta = 0.5$). The same effect was observed by Kim, Yang & Senda (2004) in their numerical study of a confined square cylinder at $Re = 3000$ and one value of confinement, $h = 4$. The fluctuating cross-stream force was 1.79 times greater in their confined case than in the corresponding unconfined case. Both studies suggest that the confined wake has a stronger global mode and stronger absolute instability than the unconfined wake.

At low Reynolds number in confined shear flows, it is important to consider how the Reynolds number is defined. The length scale is either the width of the jet/wake or the width of the duct. These two definitions are related by a factor h and, as h is varied, it is impossible to keep both constant. For a given set of results, whether confinement seems to have a stabilizing or a destabilizing effect depends on which definition of Re is chosen. A good illustration of this is found in studies of the critical Reynolds number for the onset of oscillations in the wake behind a confined circular cylinder. If the Reynolds number is defined by the width of the object, as in the experimental study of Shair *et al.* (1963) for $4 < h < 19$, then the critical Reynolds number is found to increase as the flow becomes more confined and hence confinement seems to stabilize the flow. If, however, the Reynolds number is defined by the width of the duct, as in the numerical study of Chen, Pritchard & Tavener (1995) for $0.43 < h < 9$, then the critical Reynolds number is found to decrease as the flow becomes more confined and hence confinement seems to destabilize the flow. These results are, of course, consistent with each other. The key point for this paper is that viscosity is clearly having an effect at these Reynolds numbers, which were $50 < Re < 150$. Similar results at $62 < Re < 300$ can be found in Turki, Abbasi & Nasrallah (2003), for a confined square cylinder at $3 < h < 7$ and De & Dalal (2007) for a confined triangular cylinder at $2 < h < 11$.

At intermediate Reynolds numbers, a similar example can be found in the numerical results of Davis, Moore & Purtell (1983) for the fluctuating lift coefficient on a square cylinder in a duct at $h = 3$ and $h = 5$. If the Reynolds number is based on the width of the square then, at given Reynolds number, the r.m.s. cross-stream fluctuations decrease as the flow becomes more confined, hence confinement seems to stabilize the flow. If, however, the results are re-scaled so that the Reynolds number is based on the width of the duct then, at given Reynolds number, the r.m.s. cross-stream fluctuations increase as the flow becomes more confined, hence confinement seems to destabilize the flow. Above a Reynolds number of $Re \approx 750$, however, Davis *et al.* (1983) find

that confinement is destabilizing, regardless of how the Reynolds number is defined. The key point for this paper is that, above a Reynolds number of approximately 750, viscous effects can be neglected in confined wakes. The effect of viscosity on confined jets and wakes is the subject of a paper parallel to this one (Rees & Juniper in press), which shows that the stability of a confined viscous jet/wake becomes almost identical to that of the corresponding inviscid jet/wake when $Re > 1000$.

Surface tension, at first glance, seems to act similarly to the finite shear layer thickness described earlier: it stabilizes high wavenumbers and, in a temporal analysis, this seems to be all that it does (Rayleigh 1894). A spatio-temporal stability analysis, however, reveals more interesting behaviour. As for the finite shear layer thickness, there is a single saddle point caused by the surface tension (called 's_1' in Juniper 2006). This s_1 saddle, however, is more unstable than the shear layer s_1 saddle described earlier. In particular, it can be absolutely unstable even in quite strong coflow. Physically, this is because surface tension acts similarly to an elastic sheet between the flows and, like an elastic sheet, provides a mechanism for perturbations to propagate upstream. As for the jets and wakes described earlier, there are also an infinite number of saddle points (called 's_2' in Juniper 2006) caused by the interaction between the two shear layers. When the flow is confined, a further set of s_2 saddles is introduced, caused by the interaction between the shear layers and their images. At intermediate and strong surface tensions, the s_1 saddle moves towards these s_2 saddles, creating combined saddle points that are particularly unstable. This causes the interesting interaction between length scales that was alluded to earlier in §1 and that is examined in this paper.

In a single study it would be impractical to examine every parameter that affects the stability of jets and wakes. With a reduced parameter set, however, it is important to check the applicability of the model, which is quite easy for this study. Viscosity is neglected, which means that the results will be accurate for $Re > 10^3$, reasonably accurate for $10^2 < Re < 10^3$ and inaccurate for $Re < 10^2$. Plug flow velocity profiles are assumed, which remove the stabilizing effect of finite thickness shear layers. If, therefore, the wavelength of an instability that is predicted by this model is less than $O(\delta)$, where δ is the shear layer thickness that would be expected in reality, then the instability would actually be stabilized by the finite thickness shear layer. The surface tension saddle, which has a smaller wavelength than the jet/wake column saddle, sits at $k^* \approx 2$ (from figure 2). The smallest instabilities therefore have wavelength of order πL_{ref}, where $L_{ref} \equiv \sigma/(\rho_{ref} U_{ref}^2)$ and these must be greater than $O(\delta)$ for the model to be valid.

For instance, a laboratory experiment has been designed by this group to look at the effect of confinement on jets and wakes. Confinement is expected only to affect long wavelength perturbations, of the order of the width of the streams. Surface tension has been proposed as a mechanism that could attenuate short wavelength instabilities without greatly affecting long wavelengths and also keep the two fluids separate. The experiment has the following characteristics: $\sigma \sim 0.025\,\mathrm{N\,m^{-1}}$ (silicone oil/water), $U_{av} \sim 0.1\,\mathrm{m\,s^{-1}}$, $U_{ref} \equiv \Delta U/2 \sim 0.05\,\mathrm{m\,s^{-1}}$, $h_{ref} \sim 0.01\,\mathrm{m}$, $\mu \sim 10^{-3}\,\mathrm{kg\,m^{-1}\,s^{-1}}$, $\rho \sim 10^3\,\mathrm{kg\,m^{-3}}$. In this situation, the Reynolds number is 10^3, which is high enough for the viscosity to be neglected, and the smallest unstable wavelength is of order $\pi L_{ref} \approx 0.03\,\mathrm{m}$, which is larger than the shear layer thickness where the two flows are first introduced. The model is therefore valid at the base of the flow, which is where the absolutely unstable region is expected. In this situation, Σ, which is defined in §2, is of order 1. Larger variations of Σ can be achieved by varying U_{ref}. For instance, with U_{ref} varying from 0.1 to 0.01 m s^{-1}, Σ varies from 0.25 to 25. Even
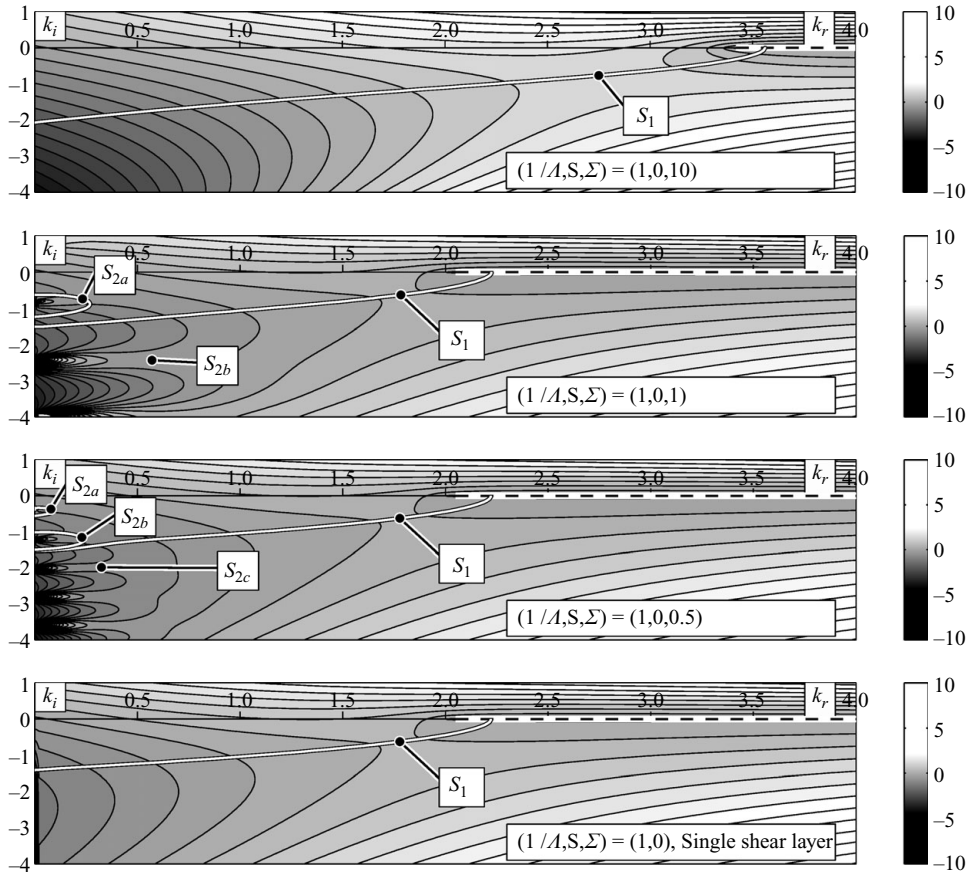
FIGURE 2. Contours of $g_i(k)$ at $(x/t, z/t) = (0,0)$ for varicose perturbations in a uniform density unconfined jet flow with surface tension. The saddle points are solutions with $\partial g / \partial k = 0$ and represent modes with zero group velocity. The integration path is shown as a solid white line. Saddle s_1 represents the surface-tension-driven instability of the single shear layer. Saddles $s_{2a}, s_{2b}, \ldots$ represent interactions between the shear layers. As Σ decreases, more of the s_2 saddles lie on the integration path until, at very low Σ, they all lie close to the k_i-axis. Contours of g_i for the single shear layer are shown for comparison.

larger variations can be achieved with different apparatus. For instance, with h_{ref} varying from 0.0025 to 0.25 m, Σ varies from 0.01 to 100. Some of these situations have low Froude number, which means that gravity, which has been neglected in this paper, would need to be included. Nevertheless, the results in this paper demonstrate that surface tension will be quite influential in the proposed laboratory experiment.

A more practical application is fuel injection. In the fuel injectors of a typical aircraft engine, a thin planar film of kerosene is injected between two faster streams of air. In this situation, $\sigma \sim 0.025\,\mathrm{N\,m^{-1}}$, $U_{ref} \sim 10\,\mathrm{m\,s^{-1}}$, $h_{ref} \sim 0.001\,\mathrm{m}$, $\mu \sim 10^{-3}\,\mathrm{kg\,m^{-1}\,s^{-1}}$, $\rho_{ref} \sim 10^3\,\mathrm{kg\,m^{-3}}$. Here, $Re \sim 10^4$, which is high enough for the viscosity to be neglected. The smallest unstable wavelength due to surface tension, however, would be of order 10^{-6} m, which is much smaller than the shear layer thickness. One can conclude that, in aircraft engines, the smallest wavelength of primary jet break up is set by the shear layer thickness, not by the surface tension. This is also the case in

rocket engines, where the surface tension is negligible because the pressure is above the critical pressure of the reactants.

In this paper, §2 describes the model and the derivation of the dispersion relations for both varicose and sinuous perturbations. Section 3 describes the theory behind the two procedures used in this study and describes the implementation of the full impulse response procedure in detail. Section 4 examines the unconfined single shear layer analytically and explores the situations where this is relevant to jets and wakes. Section 5 examines the effect of density ratio, shear and surface tension on unconfined flows over a wide range of density ratios and surface tension. Finally, §6 examines the effect of confinement and shear over a wide range of density ratios and surface tensions, which are chosen to encompass a wide range of regimes.

2. Derivation of the dispersion relations

The model (figure 1) consists of three uniform inviscid, irrotational and incompressible flows. The inner flow has density ρ_1, velocity U_1 and thickness $2h_1$ in the z-direction. The outer flows both have density ρ_2 and velocity U_2. If the outer flow is unconfined, it extends to infinity in the z-direction. If confined, it has thickness h_2 in the z-direction. All flows have infinite extent in the x-direction and are uniform in the y-direction, which is orthogonal to both x and z.

Following Drazin & Reid (1981, §21), streamfunction perturbations of the form $\psi_i(x, z, t) = \varphi_i(z; \xi) e^{i(kx - \omega t)}$ are defined in each flow such that $u_i = \partial \psi_i / \partial z$ and $w_i = -\partial \psi_i / \partial x$. Satisfying the equation of motion constrains the profile in the z-direction by the differential equation, $\partial^2 \varphi_i / \partial z^2 - \xi_\pm^2 \varphi_i = 0$, where $\xi_\pm \equiv \pm \sqrt{k^2}$. In the confined case the dispersion relation and boundary conditions are invariant under the transformation $\xi_+ \leftrightarrow \xi_-$ and it is sufficient to take $\xi = k$ (Healey 2006).

The streamfunction profiles in the z-direction for the confined flow are

$$\varphi_1 = A_1 \cosh \xi(z - h_1 - h_2) + B_1 \sinh \xi(z - h_1 - h_2), \tag{2.1}$$
$$\varphi_2 = A_2 \cosh \xi z + B_2 \sinh \xi z, \tag{2.2}$$
$$\varphi_3 = A_3 \cosh \xi(z + h_1 + h_2) + B_3 \sinh \xi(z + h_1 + h_2). \tag{2.3}$$

Flow 3 does not need to be considered further because perturbations can be decomposed into varicose disturbances (where $A_2 = 0$) and sinuous disturbances (where $B_2 = 0$). Imposing the boundary conditions at the wall, $z = h_1 + h_2$, yields $A_1 = 0$.

At $z = h_1$ the kinematic and dynamic matching conditions between the flows are

$$\Delta [\varphi_i / (U_i - \omega / k)]_-^+ = 0, \tag{2.4}$$
$$\Delta [\rho_i (U_i - \omega / k) \varphi_i']_-^+ = \Delta p, \tag{2.5}$$

where Δp is the jump in pressure across the interface as a result of surface tension. On linearizing, this is given by $\Delta p = -\sigma \partial^2 \zeta / \partial x^2$, where $\zeta(x, t)$ is the deviation of the interface away from $z = h_1$.

Eliminating A_i and B_i yields the dispersion relation $D(k, \omega) = 0$, from which the stability of the flow can be determined. For a given set of parameters, this dispersion relation is satisfied by eigenvalues (k, ω) with associated eigenfunctions $\varphi(z; \xi)$. In dimensional terms, the varicose and sinuous dispersion relations for the model in figure 1 are, respectively,

$$D = \rho_1 (U_1 - \omega / k)^2 \coth(\xi h_1) + \rho_2 (U_2 - \omega / k)^2 \coth(\xi h_2) - \sigma \xi = 0, \tag{2.6}$$
$$D = \rho_1 (U_1 - \omega / k)^2 \tanh(\xi h_1) + \rho_2 (U_2 - \omega / k)^2 \coth(\xi h_2) - \sigma \xi = 0. \tag{2.7}$$

The non-dimensional framework used here is slightly different from that in Juniper (2006). It has the following reference scales for velocity and density:

$$U_{ref} \equiv (U_1 - U_2)/2, \tag{2.8}$$
$$\rho_{ref} \equiv (\rho_1 + \rho_2)/2. \tag{2.9}$$

The reference scale for length can either be based on surface tension or on the distance between the shear layers

$$L_{ref} \equiv \sigma/(\rho_{ref} U_{ref}^2), \tag{2.10}$$
$$h_{ref} \equiv (1/h_1 + 1/h_2)^{-1}. \tag{2.11}$$

In this paper, L_{ref} is used as the reference length so that a single framework can be used for a single shear layer, for unconfined jets/wakes and for confined jets/wakes. The dimensionless variables are

$$\omega^* \equiv \omega L_{ref}/U_{ref}, \tag{2.12}$$
$$k^* \equiv k L_{ref}, \tag{2.13}$$
$$\xi^* \equiv \xi L_{ref}. \tag{2.14}$$

The dimensionless parameters are the shear ratio, the density measure, the confinement and the non-dimensional surface tension, which can also be thought of as the inverse of a shear layer separation parameter

$$\Lambda \equiv (U_1 - U_2)/(U_1 + U_2), \tag{2.15}$$
$$S \equiv (\rho_1 - \rho_2)/(\rho_1 + \rho_2), \tag{2.16}$$
$$h \equiv (h_2 - h_1)/(h_2 + h_1), \tag{2.17}$$
$$\Sigma \equiv \sigma/(h_{ref} \rho_{ref} U_{ref}^2) \equiv L_{ref}/h_{ref}. \tag{2.18}$$

For weak surface tensions, L_{ref} and Σ become very small, which can also be thought of as the shear layers becoming very far apart. It is important to note that, in this paper, the shear layers always have non-zero surface tension. This means that they always behave differently from shear layers with no surface tension, even if the surface tension is vanishingly small or, equivalently, if the walls are very far apart. To some extent this is an artefact of the model, as discussed in §1: in physical situations with small surface tension, L_{ref} may be smaller than the shear layer thickness, so that the model becomes invalid.

In non-dimensional terms, the varicose and sinuous dispersion relations become

$$D = (1 + S)(1/\Lambda + 1 - \omega^*/k^*)^2 \coth(2\xi^*/\Sigma(1 + h))$$
$$+ (1 - S)(1/\Lambda - 1 - \omega^*/k^*)^2 \coth(2\xi^*/\Sigma(1 - h)) - \xi^* = 0, \tag{2.19}$$
$$D = (1 + S)(1/\Lambda + 1 - \omega^*/k^*)^2 \tanh(2\xi^*/\Sigma(1 + h))$$
$$+ (1 - S)(1/\Lambda - 1 - \omega^*/k^*)^2 \coth(2\xi^*/\Sigma(1 - h)) - \xi^* = 0. \tag{2.20}$$

The non-dimensional framework is used in most of this paper and the asterisks are dropped. Sometimes the dimensional framework is used when drawing physical conclusions. It will be stated explicitly when this is the case to avoid any ambiguity.

The stability of the flow is determined by two modes: one where each shear layer acts individually and one where the shear layers interact. Each shear layer can interact with the other shear layer, which is at distance $2h_1$ and with its image shear layer, which is at distance $2h_2$. The characteristic length scale of the interacting mode is the smaller of h_1 and h_2. The parameter Σ and the non-dimensional framework described

above have been constructed to reflect the fact that the behaviour is dominated by the denser fluid, identified by ρ_{ref}, the smaller length scale, identified by h_{ref}, and by the relative (rather than absolute) velocity, identified by U_{ref}. The strength of the surface tension effect is determined by σ, which acts on a length scale L_{ref}.

Juniper (2006) introduced surface tension in order to regularize this problem, making it suitable for a Briggs–Bers analysis, but then tended σ to zero in order to focus on the effect of confinement. When $\sigma = 0$ (2.6) and (2.7) have several symmetries for both confined and unconfined flows. These symmetries are best understood by considering the image system of the flow with interchanged velocities, densities and length scales. When $\sigma \neq 0$, however, nearly all of these symmetries are lost. The only true symmetry that remains is for confined varicose motion, which is unchanged under the transformation $(\Lambda, S, h, \Sigma) \leftrightarrow (-\Lambda, -S, -h, \Sigma)$. Later it will be shown that other symmetries can be found in the limit $h \sim -1$.

3. Spatio-temporal stability analysis

In this paper, two procedures are used to analyse the stability of the flow. The first procedure is a conventional spatio-temporal stability analysis in which the response to an impulse is examined at the spatial point of the impulse. The system is absolutely unstable if the response grows in time and is convectively unstable or stable if the response decays in time. This procedure is used throughout the paper to determine the boundaries between absolute and convective instabilities in various parameter spaces. The second procedure is an examination of the full impulse response in the outer flow, as in Healey (2006) and Juniper (2007). This helps to identify the factors that govern the shape and stability of the wavepacket. This procedure is restricted to unconfined flows but establishes the effects of density S, shear Λ and surface tension Σ before introducing confinement.

3.1. *Evaluation of the impulse response*

In an adaptation of Huerre (2000), the full perturbation streamfunction in each fluid $(i = 1, 2, 3)$ is given by the double Fourier integral of the normal modes, each of which is multiplied by its mode shape $\varphi_i(z, \xi)$

$$\psi_i(x, z, t) = \frac{1}{(2\pi)^2} \int_{F_k} \int_{L_\omega} \hat{\psi}_i(k, \omega) \varphi_i(z; \xi) e^{i(kx - \omega t)} \, d\omega \, dk. \tag{3.1}$$

The mode shape is determined by the Rayleigh equation

$$\frac{\partial^2 \varphi_i}{\partial z^2} + \xi^2 \varphi_i = 0, \tag{3.2}$$

which, for unconfined flows, yields solutions proportional to $\exp(\pm \xi z)$ in the upper and lower z-domains, respectively. These can be incorporated into the exponential to give $\exp(i(kx \mp i\xi z - \omega t))$, as in Healey (2006).

If the forcing is an impulse that excites all modes equally at $(x, t) = (0, 0)$ then the full forcing can also be expressed as the double Fourier integral of the normal modes multiplied by their mode shapes $\varphi_i(z, \xi)$

$$S_i(x, z, t) = \frac{1}{(2\pi)^2} \int_{F_k} \int_{L_\omega} \hat{S}_i(k, \omega) \varphi_i(z; \xi) e^{i(kx - \omega t)} \, d\omega \, dk. \tag{3.3}$$

By substituting for k and ω, the dispersion relation $D(k, \omega)$ can be associated with the partial differential equation

$$D\left(-i\frac{\partial}{\partial x}, i\frac{\partial}{\partial t}\right)\psi_i(x, z, t) = S_i(x, z, t). \tag{3.4}$$

Substituting (3.1) and (3.3) into (3.4) gives the following governing equation in spectral space:

$$\hat{\psi}(k, \omega)D(k, \omega) = \hat{S}(k, \omega). \tag{3.5}$$

The impulse response can then be calculated by choosing $\hat{S}(k, \omega) = 1$ and substituting (3.5) back into (3.1).

The integration over ω is evaluated using the residue theorem and retains non-zero contributions only from those modes that satisfy the dispersion relation $D(k, \omega) = 0$. For each value of k there exist two values of ω that satisfy $D(k, \omega) = 0$ so the solution is formed from integrals over the two different branches of $\omega(k)$. These two branches share the symmetry that $\mathrm{Re}\{k_+, \omega_+\} \leftrightarrow \mathrm{Re}\{k_-, \omega_-\}$, which results in the two integrals yielding identical contributions. This makes it sufficient to consider integrating over only one of the branches

$$\psi(x, z, t) = -\frac{i}{2\pi}\int_{F_k}\frac{1}{\partial D/\partial\omega[k, \omega(k)]}e^{-igt}\mathrm{d}k \quad \text{where } g \equiv w(k) - kx/t - i\xi z/t. \tag{3.6}$$

In a conventional spatio-temporal stability analysis, g is investigated as the parameters vary, keeping $(x/t, z/t) = (0, 0)$. In an analysis of the full impulse response, g is investigated as $(x/t, z/t)$ varies, keeping the parameters constant. The evaluation of g is identical in both methods. In this paper, the second procedure is described in more detail.

Given $(x/t, z/t)$, the dominant contribution to integral (3.6) in the long-time limit comes from saddle points of the function $g(k; x/t, z/t)$. At these saddle points, where $\partial g/\partial k = 0$, the group velocity, $\partial\omega/\partial k$ is equal to $x/t + iz/t$. In other words, dominant contributions come from disturbances that travel with the same group velocity as the observer.

This restricts the investigation to following the dominant saddle point in the k-plane as $(x/t, z/t)$ varies. The dominant saddle point has the largest growth rate g_i, on the integration path. When a saddle point moves off the integration path, it no longer influences the integral at long times because its associated disturbances disperse. In the framework of a classic Briggs–Bers analysis (Briggs 1964), a saddle point moving off the integration path is equivalent to its transforming from a valid k_+/k_- pinch point to an invalid k_-/k_- pinch point.

3.2. *The positions of branch points and saddle points in the k-plane*

Both types of spatio-temporal stability analyses reduce to following saddle points in the k-plane. At this point it is worth discussing the positions of these saddle points.

The non-dimensional dispersion relation for an unconfined single shear layer with surface tension is

$$(1 + S)(1/\Lambda + 1 - \omega/k)^2 + (1 - S)(1/\Lambda - 1 - \omega/k)^2 - \xi = 0. \tag{3.7}$$

When a second shear layer is introduced, the first term gains a factor of either $\coth(2k/\Sigma(1 + h))$, for varicose interactions, or $\tanh(2k/\Sigma(1 + h))$, for sinuous interactions. Hence the first term represents the interaction of one shear layer with the other. Both $\coth(2k/\Sigma(1 + h))$ and $\tanh(2k/\Sigma(1 + h))$ give rise to a set of poles along the k_i-axis where their values become infinite. Thus, poles occur where $2k/\Sigma(1 + h) = n\pi$ (varicose) or $(n + 1/2)\pi$ (sinuous), where n is an integer.
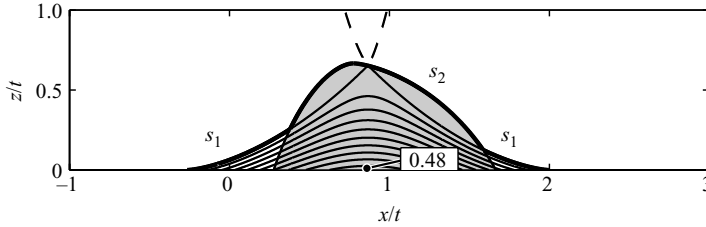
FIGURE 3. The full impulse response in the outer fluid for varicose perturbations of an unconfined double shear layer with $(1/\Lambda, S, \Sigma) = (1.5, -0.2, 0.001)$ shown as lines of constant growth rate g_i. The surface tension mode dominates at the front and back of the wavepacket and the jet/wake column mode (shaded), which propagates faster in the cross-stream direction, defines the boundary of the centre of the wavepacket. Dotted lines correspond to saddles that have moved off the integration path. The dominant saddle on the edge of the wavepacket is shown as a thick line.

When this pair of shear layers is confined, the second term gains an extra factor of $\coth(2k/\Sigma(1-h))$, whether the two shear layers are interacting in a varicose or in a sinuous manner. This term scales with the outer flow width and represents the interaction of a shear layer with its image, which is always varicose. The additional $\coth(2k/\Sigma(1-h))$ term also gives rise to a further set of poles along the k_i-axis where its value becomes infinite. Thus, poles occur where $2k/\Sigma(1-h) = n\pi$, where n is an integer.

The last term in the dispersion relation relates to the pressure jump due to the surface tension and represents the instability of each individual shear layer due to surface tension. It remains the same when a second shear layer is introduced and when the flow is confined. This term gives rise to a pair of branch points on the k_r-axis. One branch point is located at infinity and the other on the positive k_r-axis at distance $2(1 - S^2)$ from the origin, for low Σ. The location at high Σ is given by the right-hand side of (6.3).

The arrangement of poles leads to a cascade of saddle points just off the k_i-axis, as noted by Juniper (2006) for confined jets and wakes, and Healey (2007) for the confined rotating disk boundary layer. These saddle points represent modes that arise from interactions of the shear layers with each other and with their images $(s_{2a}, s_{2b}, \ldots)$, and are referred to as jet/wake column modes. Their position is dictated by the parameters h and Σ, which cause them to shift up and inwards towards the origin or down and outwards away from the origin. Another saddle point (s_1) arises near the surface tension branch point. This saddle point represents the surface-tension-driven single shear layer instability and is referred to as the surface tension saddle.

Initially, the integration path in (3.6) is placed along the k_r-axis. The method of steepest descent is used to approximate the integral in the long-time limit. This involves deforming the integration path over valid k^+/k^- saddle points, always along contours of $g_r = const$. The integration path passes over several saddle points down the k_i-axis, picking up contributions from jet/wake column modes. From one saddle point to the next the path descends into deep wells, where g_i takes very low values. At these points the path jumps onto the g_r-contour that passes over the next saddle point. The path continues like this until a g_r contour is taken that passes out over the s_1 saddle point picking up the contribution from the surface tension mode, as shown in figure 2.

3.3. *The full impulse response*

The impulse response is visualized by plotting contours of the growth rate g_i in the $(x/t, z/t)$-plane (figure 3). The zero-growth rate contour, on which $g_i = 0$, marks the

outline of the unstable wavepacket in the $(x/t, z/t)$-plane. Within the wavepacket the impulse response grows exponentially whereas outside it decays exponentially. The growth rate at the origin determines the nature of instability. If the origin is contained within the wavepacket then the flow is absolutely unstable. If it is not contained within the wavepacket then the flow is convectively unstable. Finally, if there is no growing wavepacket then the flow is stable. The procedure used to produce these wavepacket visualizations is outlined below.

For an initial value of $(x/t, z/t)$, plots of g_i are calculated in k-space, as shown in figure 2. The dominant saddle point is identified visually and the saddle point is followed as x/t and z/t vary until g_i reaches the value of the contour that is to be traced. Then the saddle is followed as x/t and z/t vary while keeping g_i constant. During this process, saddle points can move off the integration path. These transition points are identified afterwards by plotting g_i in k-space around these points along the contour. They are shown in figure 3 by the transition from a solid line (where the saddle is on the integration path) to a dashed line (where it is not).

Different saddle points can dominate in different regions of the wavepacket. During transition between these regions, a second subdominant saddle point moves onto the integration path and then becomes the dominant saddle point. Figure 3 shows an absolutely unstable wavepacket taken for values $(\Lambda, S, \Sigma) = (1.5, -0.2, 0.001)$. The surface tension saddle point dominates the front and back of the wavepacket with short wavelength disturbances. It also dominates in the interior of the wavepacket at slightly longer wavelengths and with large growth rates. The principal jet/wake column mode saddle point represents long wavelength disturbances with low growth rates. These travel with faster transverse velocities than those of the surface tension mode and hence define the central boundary of the wavepacket.

4. Analytic solutions for an unconfined single shear layer

In the first half of this section, an unconfined single shear layer with surface tension is studied analytically. When a second shear layer is introduced or the flow is confined, closed-form solutions in k cannot be derived and it is impossible to determine analytical criteria for absolute instability. In the second half of this section, however, the results for the unconfined single shear layer are shown to be relevant for confined jets and wakes in ways that depend on whether $\Sigma \ll 1$, $\Sigma \sim 1$ or $\Sigma \gg 1$.

4.1. *Analysis of the unconfined single shear layer*

In its dimensional form the dispersion relation for the unconfined single shear layer is

$$D = \rho_1(U_1 - \omega/k)^2 + \rho_2(U_2 - \omega/k)^2 - \sigma\xi = 0. \tag{4.1}$$

This has been included as a reference to help introduce the physical concept of apparent density later on in this section. This is algebraic in ω, k and can be solved for ω analytically. In its dimensionless form, the dispersion relation is given by (3.7).

Saddle points satisfy the equation $\partial\omega/\partial k = 0$, which is equivalent to the statement $\partial D/\partial k = 0$ as long as $\partial D/\partial\omega \neq 0$ because $dD/dk = \partial D/\partial k + (\partial\omega/\partial k)\partial D/\partial\omega = 0$. Hence saddle points of the unconfined single shear layer with surface tension also satisfy

$$k\frac{\partial D}{\partial k} = 2(1 + S)(1/\Lambda + 1 - \omega/k)(\omega/k) + 2(1 - S)(1/\Lambda - 1 - \omega/k)(\omega/k) - \xi = 0. \tag{4.2}$$

The mass flux M and momentum flux J are defined as $M \equiv (1/2)(\rho_1 U_1 + \rho_2 U_2)/(\rho_{ref} U_{ref}) = 1/\Lambda + S$, and $J \equiv (1/2)(\rho_1 U_1^2 + \rho_2 U_2^2)/(\rho_{ref} U_{ref}^2) = 1/\Lambda^2 + 2S/\Lambda + 1$. When the real part of k is positive, which can be confirmed *a posteriori*, $\xi = k$ and (3.7) and (4.2) then simplify to quadratics in ω/k, which is given the symbol c

$$2c^2 - 4Mc + 2J - k = 0, \tag{4.3}$$

$$4c^2 - 4Mc + k = 0. \tag{4.4}$$

Conducting a temporal stability analysis on (4.3) gives

$$c = M \pm \left(\frac{1}{2}k - J - M^2\right)^{1/2} \tag{4.5}$$

$$= 1/\Lambda + S \pm \left(\frac{1}{2}k - (1 - S^2)\right)^{1/2}. \tag{4.6}$$

Hence unstable wavenumbers exist for $0 < k < 2(1 - S^2)$. This indicates that at large density differences, for which S is close to ± 1, the unstable modes of the flow are restricted to smaller wavenumbers than at small density differences, for which S is close to 0. Transforming to a dimensional framework, this range of unstable wavenumbers scales with σ^{-1} because k is non-dimensionalized with respect to L_{ref}.

In the spatio-temporal stability analysis, the position of the saddle point can be found by solving (4.3) and (4.4) for c, k and ω. This gives

$$c = \tfrac{2}{3}(1 \pm Q^{1/2})M, \tag{4.7}$$

$$k = \tfrac{8}{9}(1 - 2Q \mp Q^{1/2})M^2, \tag{4.8}$$

$$\omega = \tfrac{16}{27}(1 - 3Q \mp 2Q^{3/2})M^3, \tag{4.9}$$

where $Q \equiv 1 - 3J/4M^2$. When $Q > 0$, c, k and ω are all real and so the saddle point is located on the k_r-axis with $\omega_i = 0$. When $Q < 0$, the saddle point is located off the k_r-axis with $\omega_i > 0$. Therefore the transition between convective and absolute instabilities occurs when $Q = 0$ corresponding to $3J = 4M^2$. Noting that $J = M^2 - S^2 + 1$, this can be re-arranged as

$$\tfrac{1}{3}M^2 + S^2 = 1, \tag{4.10}$$

which is an ellipse in (M, S)-space. Equation (4.10) can also be written as

$$\tfrac{1}{3}(1/\Lambda + S)^2 + S^2 = 1, \tag{4.11}$$

which is an ellipse in $(1/\Lambda, S)$-space.

4.2. *Relevance of the stability of an unconfined single shear layer*

When $\Sigma \ll 1$, the s_2 saddles in figure 2 shrink towards the k_i-axis. The integration path passes over the s_1 saddle and over the uppermost s_2 saddles (those that lie between $k_i = 0$ and the value of k_i where the integration path intersects the k_i-axis). The impulse response is therefore a superposition of a short wavelength rapidly growing surface tension mode (s_1), for which the shear layers act independently, and a long wavelength slowly growing jet/wake column modes (s_2), for which the shear layers interact with each other. As $\Sigma \to 0$, the growth rates of the jet/wake column modes (s_2) tend to zero and the behaviour of the model tends towards that of the surface tension mode of the independent shear layers (s_1). In other words, the stability behaviour becomes that of the unconfined single shear layer in §4.1. This is also seen in the form of the dispersion relation: as $\Sigma \to 0$, both $\coth(2\xi^*/\Sigma(1 \pm h))$ and

$\tanh(2\xi^*/\Sigma(1+h))$ tend to 1, away from the k_i-axis where the surface tension saddle is located. This means that both (2.19) and (2.20) tend towards the dispersion relation for the unconfined single shear layer (3.7) away from the k_i-axis. It is important to note that the third term on the left-hand side of (3.7) represents the surface tension. It does not disappear because Σ, although small, is not equal to zero. This is quite different from the case with $\Sigma = 0$, which was examined by Yu & Monkewitz (1990). In this situation, there is no surface tension saddle (s_1) and only the jet/wake column modes (s_2) contribute. The $\Sigma \ll 1$ case is useful as a bound for the case where $\Sigma \sim 1$.

When $\Sigma \sim 1$, the shear layers interact with each other and with the walls. In this regime the concept of apparent densities is useful. For varicose perturbations, the following apparent densities are introduced: $\varrho_1 = \rho_1 \coth(2\xi/\Sigma(1+h))$ and $\varrho_2 = \rho_2 \coth(2\xi/\Sigma(1-h))$. For sinuous perturbations they are: $\varrho_1 = \rho_1 \tanh(2\xi/\Sigma(1+h))$ and $\varrho_2 = \rho_2 \coth(2\xi/\Sigma(1-h))$. Substituting into (2.6) and (2.7), respectively, reduces both equations to

$$D = \varrho_1(U_1 - \omega/k)^2 + \varrho_2(U_2 - \omega/k)^2 - \sigma\xi = 0, \qquad (4.12)$$

which is identical to the dimensional single shear layer in (4.1). The new densities depend on the variable k but behave like the single shear layer if the arguments of the hyperbolic functions are large. Using the analytic solution in k for the single shear layer as a first-order approximation, predictions can be made as to when interactions between the shear layers and the walls will start to affect the absolute/convective transition boundary. The hyperbolic functions begin to vary away from 1 when their arguments are $O(1)$. This occurs when $|h| \sim 16M^2/(9\Sigma) - 1$. This concept of apparent density is returned to in §§ 5 and 6.

When $\Sigma \gg 1$, the dispersion relations recover a form similar to the unconfined single shear layer, which can also be solved analytically. This is covered in § 6.1.

5. Effect of density measure, shear and surface tension on unconfined jets and wakes

In this section, the effect of density measure S, shear Λ and surface tension Σ are examined on unconfined jets and wakes. A conventional spatio-temporal stability analysis is performed in the first half of the section. This shows how the regions of absolute instability in parameter space change as these parameters vary. These changes are then explained in the second half of the section by performing a full impulse response analysis.

5.1. *Conventional spatio-temporal analysis*

The varicose and sinuous dispersion relations for an unconfined double shear layer flow are found by allowing h to tend to 1 in (2.19) and (2.20), respectively, to give

$$(1+S)(1/\Lambda + 1 - \omega/k)^2 \coth(\xi/\Sigma) + (1-S)(1/\Lambda - 1 - \omega/k)^2 - \xi = 0, \quad (5.1)$$
$$(1+S)(1/\Lambda + 1 - \omega/k)^2 \tanh(\xi/\Sigma) + (1-S)(1/\Lambda - 1 - \omega/k)^2 - \xi = 0. \quad (5.2)$$

Note that in the limit $h \to 1$, the length scale $h_{ref} \to h_1$ and the jet/wake column modes arising from $\coth(\xi/\Sigma)$ and $\tanh(\xi/\Sigma)$ scale with the thickness of the inner flow, as expected.

Figure 4 shows the convective/absolute transition boundaries for varicose (*a,c,e*) and sinuous (*b,d,f*) perturbations of an unconfined shear flow. The region that is absolutely unstable to the s_2 saddle points when $\Sigma = 0$ was calculated in Juniper (2006) and is shaded dark grey. This is the same as that calculated by Yu &
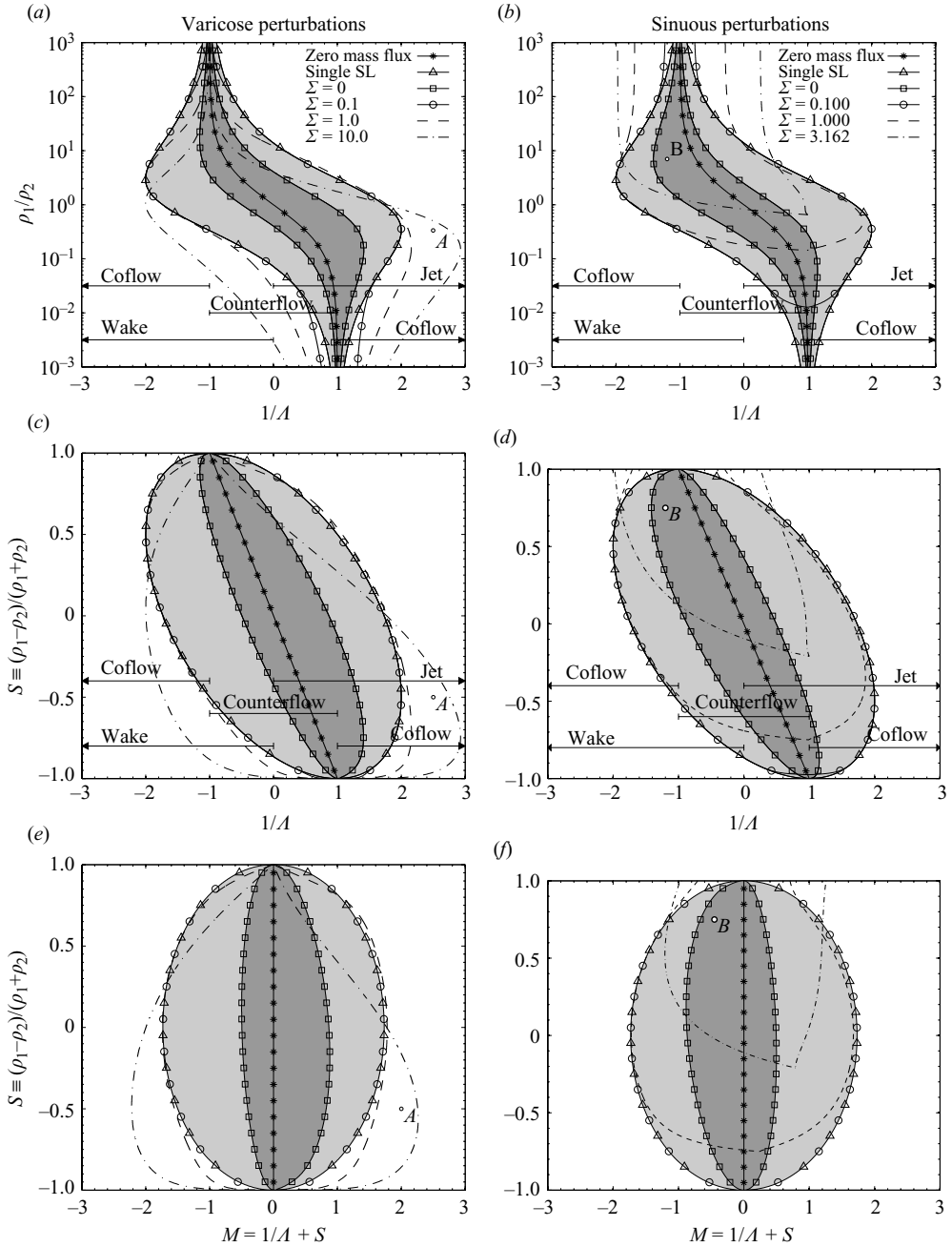
FIGURE 4. Regions of absolute instability for (a,c,e) varicose and (b,d,f) sinuous perturbations of an unconfined jet/wake flow at discrete values of surface tension Σ. In (a) and (b), these regions are shown in the ($1/\Lambda$, ρ_1/ρ_2)-plane and can be compared directly with Juniper (2006). (c) and (d) show the same data in the ($1/\Lambda$, S)-plane and (e) and (f) show the same data in the (M, S)-plane. The absolutely unstable region of the single shear layer with surface tension is shown in light grey. The absolutely unstable region of the double shear layer without surface tension is shown in dark grey. The most notable effect of surface tension is to increase the absolute instability of low density varicose jets/wakes.

Monkewitz (1990) but extends to higher $|S|$. Furthermore, the horizontal axis is $1/\Lambda$ rather than Λ, so that the absolutely unstable region is simply connected. The absolutely unstable region for the single shear layer with $\Sigma \neq 0$ was calculated in §4.1 and is shaded light grey. In figure 4, the same data are presented in three different ways: firstly in the $(1/\Lambda, \rho_1/\rho_2)$-plane, which can be compared directly with Juniper (2006); secondly in the $(1/\Lambda, S)$-plane, which is the format preferred in this paper; thirdly in the (M, S)-plane, which shows that the absolutely unstable region is an ellipse centred on the zero net mass flux line.

At low surface tensions, the wavelength of the most unstable mode is very small compared with the distance between the shear layers and therefore the shear layers do not interact. The instability is dominated by the individual shear layers, which is evident from the fact that, for both varicose and sinuous perturbations at $\Sigma = 0.1$, the absolutely unstable region is nearly identical to that of the single shear layer.

For varicose perturbations, increasing Σ causes the absolutely unstable region to shift to lower density measures, S. For sinuous perturbations, increasing Σ causes absolutely unstable regions to shift to higher density measures, S.

The point at which surface tension starts to affect the stability of the jet/wake column mode can be predicted analytically. When $\Sigma \ll 1$, the jet/wake column mode (s_2) saddles are bunched close to the k_i-axis, far away from the dominant surface tension (s_1) saddle in figure 2(c). Increasing Σ causes the jet/wake column mode saddles to move towards the surface tension saddle and interact with it. Using the analytic expression for the position of the surface tension saddle point discussed in §4, this predicts that the interaction will start when $\Sigma \sim 8M^2/9$. This can be seen in figures 4(e) and 4(f). For $\Sigma = 1$ around $S \sim 0$ the transition boundaries match those of the single shear layer. Here $M \approx \pm 1.5$ and so $8M^2/9 > 1$, i.e. there is no interaction. Around $S \sim \pm 1$, however, the transition boundaries deviate from those of the single shear layer. Here $M \approx \pm 1$ and so $8M^2/9 < 1$, i.e. there is interaction. Similarly, for $\Sigma = 10$ there is even greater interaction but for $\Sigma = 0.1$ there is very little.

5.2. *Full impulse response analysis*

The features of figure 4 can be explained by examining the full impulse response in the outer fluid (figure 3). Changing Λ simply shifts the wavepacket left or right but changing S and Σ changes the shape of wavepacket both qualitatively and quantitatively.

5.2.1. *Effect of density measure S*

Here, the effect of density measure S, is investigated by considering the full impulse response of a varicose jet whose inner flow velocity is five times that of the outer flow ($1/\Lambda = 1.5$). The full impulse responses (figure 5) are plotted at very low surface tension ($\Sigma = 0.001$). At these values of Σ there is no interaction between the jet/wake column mode (s_2) saddle and the surface tension (s_1) saddle. The individual contribution of each saddle to the full impulse response can easily be distinguished. For example in figure 5(a), the outer boundary of the impulse response is determined by the jet/wake column mode (the spiral-shaped line) and the surface tension response is contained completely inside this (at the foot of the dotted lines).

The jet/wake column mode (s_2) responses are the same as those plotted by Juniper (2006) with $\Sigma = 0$ so this section focuses on the behaviour of the surface tension (s_1) responses. The front and back of the surface tension response are the points along the x/t-axis where the growth rate due to this saddle equals 0. At these points the surface tension saddle (s_1) lies on the branch cut along the k_r-axis (figure 2). At the
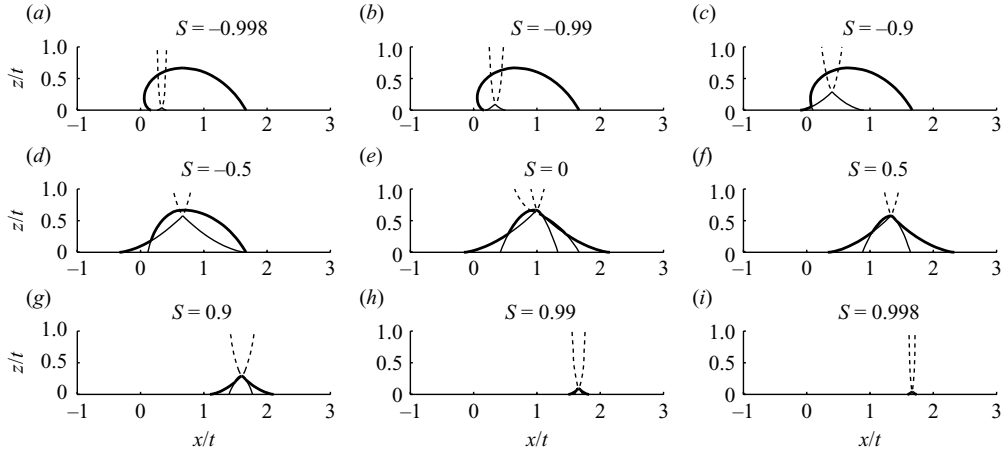
FIGURE 5. Plots of the full impulse response at $1/\Lambda = 1.5$ for varicose perturbations of an unconfined flow at density measures between $S = -0.998$ and 0.998. The wavepacket has contributions from the surface tension mode (s_1) and the jet/wake column mode (s_2). At this value of shear Λ, the jet/wake column modes are always convectively unstable. However, in (*c*), (*d*) and (*e*) the flow is made absolutely unstable by the surface tension mode. At extreme density measures the contribution from surface tension is concentrated in the x/t-axis around the velocity of the denser flow and propagates slowly in the z-direction. At moderate density measures it is spread in the x/t-axis between the two mean flow velocities and propagates more quickly in the z-direction. The shape of the impulse response in (*h*) and (*i*) is similar to that found in (*g*).

front, the saddle tends onto the axis from above, and at the back, from below. The centre of the surface tension response is the point in the $(x/t, z/t)$-plane that has the largest growth rate, g_i. For varicose perturbations, this point lies on $z/t = 0$ at

$$x/t = \frac{\rho_1 \coth(kh_1)U_1 + \rho_2 U_2}{\rho_1 \coth(kh_1) + \rho_2} U_{ref}^{-1} = \frac{\varrho_1 U_1 + \varrho_2 U_2}{\varrho_1 + \varrho_2} U_{ref}^{-1}. \tag{5.3}$$

For sinuous perturbations, $\coth(kh_1)$ is replaced by $\tanh(kh_1)$. At the centre of the wavepacket, the surface tension saddle crosses the k_r-axis between the origin and the surface tension branch point. Here, k_r is a minimum and the growth rate, which is a maximum, is given by $g_i = \omega_i - k_r x/t$. This corresponds to the disturbance with the longest wavelength and it travels solely in the x-direction. When $\Sigma \ll 1$, which corresponds to $k_r h_1 \gg 1$, both $\coth(kh_1)$ and $\tanh(kh_1)$ are approximately 1 and the position of the centre of the wavepacket simplifies to

$$x/t = \frac{\rho_1 U_1 + \rho_2 U_2}{\rho_1 + \rho_2} U_{ref}^{-1} \equiv 1 + S\Lambda \equiv M. \tag{5.4}$$

For example, at $S = -0.998$ (5.4) predicts that the centre of the surface tension response is at $x/t = 0.33$. For $S = 0.998$, it predicts that it is at $x/t = 1.67$. This expression agrees very well with figure 5 in which the impulse response is plotted at $1/\Lambda = 1.5$.

The apparent density can be used to explain why, for varicose perturbations, the region of absolute instability in figure 4 shifts to lower S as the surface tension increases. When $k_r h_1 \leqslant 1$, $\varrho_1 > \rho_1$ and the instability is similar to that of the unconfined single shear layer with a density ratio of $(\varrho_1 - \varrho_2)/(\varrho_1 + \varrho_2)$, which is greater than S. As Σ increases, $k_r h_1$ decreases further and the apparent density of the inner flow ϱ_1 increases further. Hence unconfined varicose perturbations correspond to the

unconfined single shear layer instability with a higher density measure and this effect increases as the surface tension increases. An equivalent argument explains why, for sinuous perturbations, the region of absolute instability in figure 4 shifts to higher S as the surface tension increases.

The centre of the wavepacket is defined as the point on the x/t-axis where the growth rate is a maximum, which is the centre of the surface tension response. At extreme density ratios ($S < -0.9$ and $S > 0.9$), the centre of the wavepacket becomes highly concentrated around the velocity of the denser fluid. This can be seen in figures 5(a), 5(b), 5(h) and 5(i), which are calculated at density ratios of $S = -0.998, -0.9, 0.9, 0.998$, respectively. At $S = -0.998$ the wavepacket is centred around $x/t = 0.33$, while at $S = 0.998$ the wavepacket is centred around $x/t = 1.67$. In this regime the denser fluid completely dictates the velocity of the wavepacket. The flow can only become absolutely unstable if the denser fluid is nearly stationary. This explains the convergence of absolutely unstable regions about $1/\Lambda = 1$ and -1 in figure 4(a–d), at low Σ and extreme density ratios.

At moderate density ratios ($-0.9 < S < 0.9$), the wavepacket is influenced by both fluids. The denser fluid still has the greatest influence over the shape and position of the wavepacket. However, the wavepacket is broader in the x/t-direction and extends further in the z/t-direction than at extreme density ratios. It is centred according to expression (5.4). If the denser fluid has a higher velocity than the less dense fluid then the front of the wavepacket changes little under density variations. If the denser fluid has a lower velocity than the less dense fluid then the back changes little. At uniform density ($S = 0$) both flows share equal influence and the wavepacket is broadest in the x/t-direction. Consequently, the regions of absolute instability are broadest in the moderate density ratio range.

5.2.2. *Effect of surface tension Σ*

Two points in figure 4, A and B, are examined as the surface tension is increased. Point A is for varicose perturbations at $(1/\Lambda, S) = (2.5, -0.5)$. The full impulse response is plotted for these parameter values as Σ is increased in figure 6(a).

At zero surface tension (figure 6a (i)) the only contribution to the impulse response is from the jet/wake column mode (s_2). At small surface tensions (figure 6a (ii,iii)) the impulse response also has contributions from the surface tension mode (s_1) but these saddles do not interact. At these surface tensions, long wavelength oscillations due to the jet/wake column mode propagate away from the shear layer relatively quickly but are not absolutely unstable. Short wavelength oscillations due to the surface tension mode extend at the front and the back of the wavepacket. They propagate away from the shear layer relatively slowly but can be absolutely unstable at these parameter values. Low surface tension always enlarges the region of absolute instability in the $(1/\Lambda, S)$-plane.

At intermediate surface tensions (figure 6a (iv,v)) only one saddle point lies on the integration path throughout most of the wavepacket. This saddle can appear to be either the surface tension saddle or the jet/wake column saddle, depending on the route taken through parameter space as the surface tension is increased. It is more accurate to call this the combined saddle because it represents interaction of the two modes. The back of the wavepacket has the characteristics of the surface tension mode but the centre and front have characteristics of the jet/wake column mode.

At very high surface tensions (figure 6a (vi)) only one saddle point contributes to the impulse response. Its growth rate decreases as Σ increases until the flow becomes completely stable.
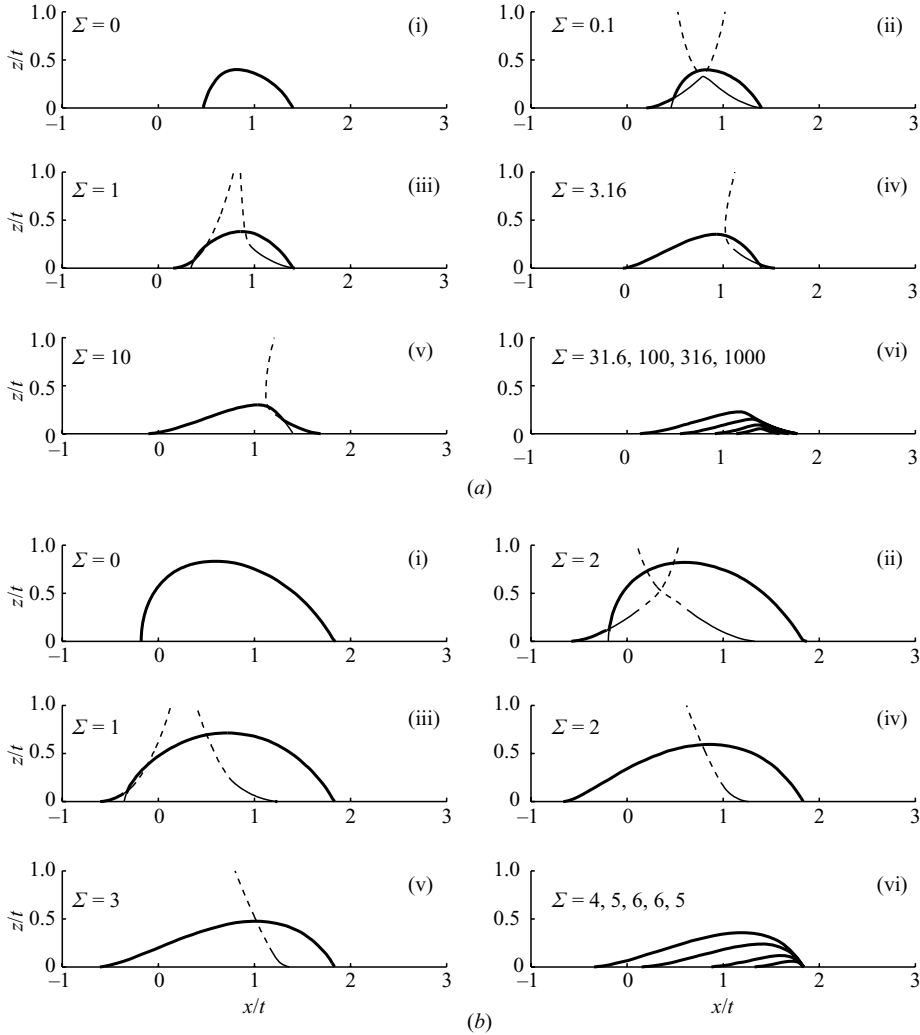
FIGURE 6. Plots of the impulse response in the outer fluid for (*a*) point A in figure 4, which is a varicose jet at $(1/\Lambda, S) = (2.5, -0.5)$ and (*b*) point B, which is a sinuous wake at $(1/\Lambda, S) = (-1.1, 0.75)$, for a range of surface tensions, Σ. Initially, both flows become more unstable as the surface tension increases. At high surface tension, however, they both are stabilized.

Point B is for sinuous perturbations at $(1/\Lambda, S) = (-1.1, 0.75)$. At zero surface tension, this flow is absolutely unstable. As the surface tension increases, the behaviour is similar to that seen at point A. The behaviour at both points demonstrates that surface tension has both a destabilizing and a stabilizing effect on jets and wakes. At low and intermediate surface tensions, it destabilizes these flows. At high surface tensions, it stabilizes them.

6. Effect of confinement on shear flows with surface tension

In this section, a conventional spatio-temporal analysis is used to determine the regions of absolute instability as a function of shear and confinement $(1/\Lambda, h)$ at seven

values of density measure S, and four values of surface tension Σ. These values cover the transition from the weak surface tension regime, where the single shear instability dominates, to the strong surface tension regime, where there is strong interaction between the boundaries and the shear layer. The results are shown in figures 7 and 8. In the first part of this section, the limit $\Sigma \to \infty$ is studied analytically as a bound for the $\Sigma \gg 1$ results. In the second part, results are presented for general surface tensions.

6.1. *Strong surface tension limit*

When $\Sigma \gg 1$, surface tension forces are much more significant than inertial forces. Short wavelength disturbances are strongly stabilized, so unstable modes have wavelengths of order L_{ref}, which are much larger than the width of either flow, of order h_{ref}. In this limit, the hyperbolic functions in the confined varicose and sinuous dispersion relations (2.19) and (2.20) can be approximated by the leading-order term in their Taylor expansions. This reduces the dispersion relations to algebraic expressions in ω and k, which can be solved analytically.

As $\Sigma \to \infty$, the function $\coth(2\xi/\Sigma(1 \pm h))$ tends to $\Sigma(1 \pm h)/2\xi$. Consequently, the varicose dispersion relation (2.19) reduces to

$$D = \frac{\Sigma(1 + S)(1 + h)(1/\Lambda + 1 - \omega/k)^2}{2\xi} + \frac{\Sigma(1 - S)(1 - h)(1/\Lambda - 1 - \omega/k)^2}{2\xi} - \xi = 0. \tag{6.1}$$

Physically, the first two terms in (6.1) give the pressure fluctuations in the inner and outer flows while the last term gives the jump in pressure across the interface. Both pressure fluctuations are $O(\Sigma)$, which is important for two reasons. Firstly they are large enough to overcome the strong surface tension at long wavelengths and secondly they can compete equally with each other in order to sustain oscillations to the interface. The dispersion relation retains the confined varicose symmetry $(\Lambda, S, h, \Sigma) \leftrightarrow (-\Lambda, -S, -h, \Sigma)$ and gains the symmetry $(S, h) \leftrightarrow (h, S)$. In other words, the density measure and the confinement are interchangeable. This allows the confinement to be combined with the density measure using the concept of apparent density introduced in §4.2.

In order to formulate (6.1) in terms of apparent density, new reference scales are introduced: $h'_{ref} \equiv (h_1 h_2)^{1/2}$, which is the geometric average of the two cross-stream length scales of the flows; $L'_{ref} \equiv (\sigma h'_{ref}/\rho'_{ref} U_{ref}^2)^{1/2}$, which is the geometric average of h'_{ref} and the surface tension length scale; density, $\rho'_{ref} \equiv (\rho_1/h_1 + \rho_2/h_2)h'_{ref}/2$, in which the density is weighted by the thinness of each flow. The new dimensionless variables are $\omega' \equiv \omega L'_{ref}/U_{ref}$, $k' \equiv k L'_{ref}$ and $\xi' \equiv \xi L'_{ref}$. The new dimensionless parameter is $S' \equiv (S + h)/(1 + Sh) \equiv (\rho_1/h_1 - \rho_2/h_2)/(\rho_1/h_1 + \rho_2/h_2)$. Under these transformations the varicose dispersion relation at large Σ (6.1) becomes

$$D = (1 + S')(1/\Lambda + 1 - \omega'/k')^2 + (1 - S')(1/\Lambda - 1 - \omega'/k')^2 - \xi'^2 = 0. \tag{6.2}$$

Equation (6.2) is almost identical to the dispersion relation for an unconfined single shear layer (4.12). The two expressions differ only by the last term: in the unconfined case this term is ξ and in the large Σ case it is ξ'^2. Performing a temporal instability analysis gives unstable wavelengths for $0 < \xi'^2 < 2(1 - S'^2)$. Transforming back into the original non-dimensional variables gives

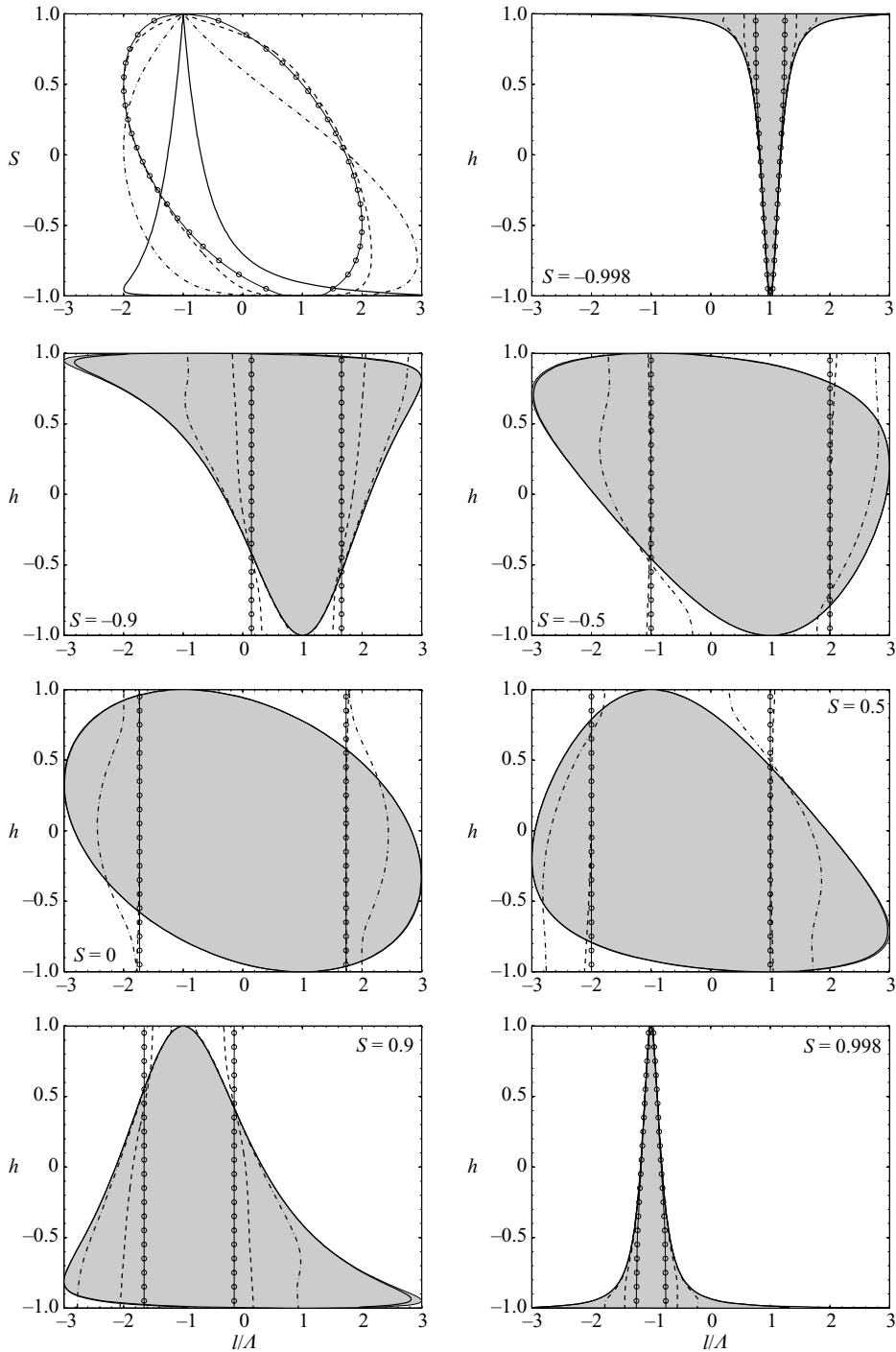$$0 < \xi < \sqrt{(1 - S^2)(1 - h^2)\frac{(1 - Sh)}{(1 + Sh)^2}\Sigma}. \tag{6.3}$$

FIGURE 7. Convective/absolute instability transition boundaries for varicose perturbations of a confined jet/wake shear flow as a function of shear Λ, density ratio S, confinement h and surface tension Σ. The top left figure is the unconfined case for $\Sigma = 0.1$ (circle), 1 (dashed), 10 (dot-dashed), 1000 (solid). The remaining figures show $(1/\Lambda, h)$-plane at given density measures. At every density ratio and surface tension, confinement causes absolute instability to occur at lower shear than the unconfined case. The shaded regions are absolutely unstable regions calculated analytically for the strong surface tension limit $\Sigma \gg 1$.
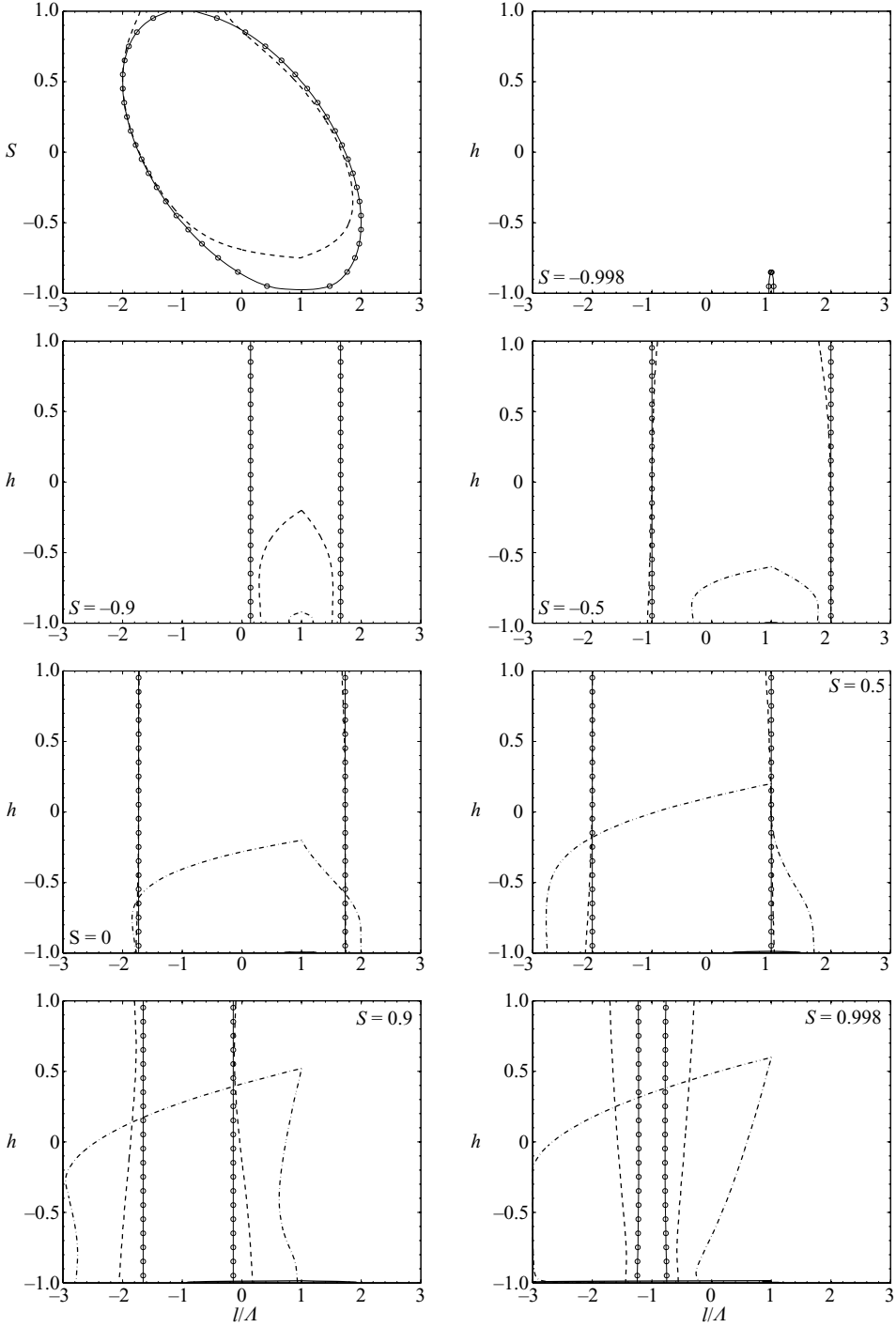
FIGURE 8. Convective/absolute instability transition boundaries for sinuous perturbations of a confined jet/wake shear flow as a function of shear Λ, density ratio S, confinement h and surface tension Σ. The top left figure is the unconfined case for $\Sigma = 0.1$ (circle), 1 (dashed), 10 (dot-dashed), 1000 (solid). The remaining figures show $(1/\Lambda, h)$-plane at given density measures. At every density ratio and surface tension, confinement causes absolute instability to occur at lower shear than the unconfined case. The shaded regions are absolutely unstable regions calculated analytically for the strong surface tension limit $\Sigma \gg 1$.

This indicates that the flow is stabilized whenever S or h equals ± 1. Transforming to a dimensional framework, this range of unstable wavenumbers scales with $\sigma^{-1/2}$ because k is non-dimensionalized with respect to L_{ref}. This result at high Σ differs from that at low Σ, in which ξ scales with σ^{-1}.

For the unconfined single shear layer, the denser flow has more influence than the less dense flow on the velocity of the unstable wavepacket. The reference density $\rho_{ref} = (\rho_1 + \rho_2)/2$ was constructed accordingly to pick out the density of the dominant fluid. When the surface tension is strong, unstable modes have wavelengths that are much larger than the width of either flow, which means that both the confining wall and the presence of the other shear layer are influential. In this case, the dominant flow is determined by the denser of the two flows weighted by the inverse of its width. The new reference density $\rho'_{ref} = (\rho_1/h_1 + \rho_2/h_2)h'_{ref}/2$ has been constructed accordingly. As was seen in §4.2, confining each flow has a strong effect on the apparent density of that flow, with a corresponding effect on the instability. In the large Σ regime, the dispersion relation yields a single saddle point in complex k-space satisfying the equation

$$c = \tfrac{3}{4}(1 \pm Q'^{1/2})M', \tag{6.4}$$

where $Q' \equiv 1 - 8J'/9M'^2$ and J', M' are defined with the new reference density. As before, the convective/absolute instability transition occurs when $Q' = 0$, corresponding to $8J' = 9M'^2$. This gives a general absolute/convective transition criteria involving shear, density measure and confinement: $(1/\Lambda, S, h)$. Noting that $J' = M'^2 - S'^2 + 1$, this can be re-arranged as

$$\tfrac{1}{8}M'^2 + S'^2 = 1. \tag{6.5}$$

This is an equation for an ellipse in (M', S')-space. By maximizing $1/\Lambda$ with respect to S' it is found that the lowest shear at which absolute instability occurs is at $1/\Lambda = \pm 3$, corresponding to $S' \equiv (S + h)/(1 + Sh) = \mp 1/3$. This gives a general relation between S and h for the configuration that requires least shear to achieve absolute instability. For jets, where $1/\Lambda$ is positive, S' is equal to $-1/3$ and for wakes, where $1/\Lambda$ is negative, S' is equal to $1/3$. Consequently, for a given density measure S, the optimal values of confinement h are given by

$$h = -\frac{1 + 3S}{3 + S} \quad \text{for jets} \tag{6.6}$$

$$h = +\frac{1 - 3S}{3 - S} \quad \text{for wakes} \tag{6.7}$$

Absolutely unstable regions predicted from (6.4) are shaded light grey in figure 7 at every value of the density measure. They show excellent agreement with the numerical calculations at $\Sigma = 1000$ (the thick solid line). When $S = 0$ (figure 7e), which corresponds to $S' = h$, (6.2) gives rise to an elliptic absolutely unstable region in $(1/\Lambda, h)$-space in the same way as (4.1) gave rise to an elliptic region in $(1/\Lambda, S)$-space. An identical absolutely unstable region exists in $(1/\Lambda, S)$-space when $h = 0$, corresponding to $S' = S$ by symmetry. Furthermore, whenever either S or h is equal to ± 1, corresponding to $S' = \pm 1$, either the inner or outer pressure fluctuations vanish and no absolutely unstable regions exist (in fact the flow is stable). This agrees with the fact that the wavepacket is stabilized as $\Sigma \to \infty$ in the unconfined case ($h = 1$).
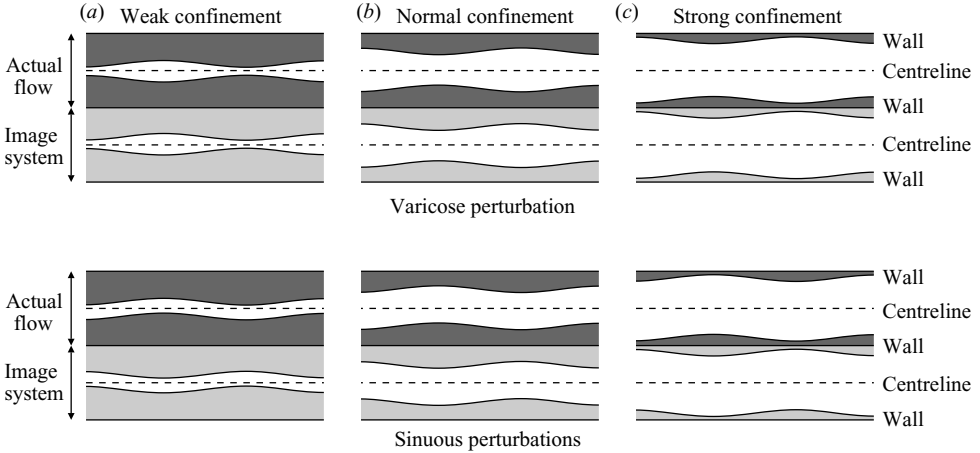
FIGURE 9. Image systems of confined varicose and sinuous flows under (*a*) weak confinement, (*b*) normal confinement and (*c*) strong confinement. In (*a*) the lower shear layer in the actual flow is most influenced by the other shear layer in the actual flow. In (*b*) the same shear layer is equally influenced by both the other shear layer and its image on the wall. In (*c*) the shear layer is most influenced by its image on the wall, which always interacts with it in a varicose manner. Both varicose and sinuous perturbations in the strongly confined flow in (*c*) are similar to varicose perturbations in the weakly confined flow in (*a*). This can be visualized by interchanging the walls with the centrelines and the inner fluid with the outer fluid corresponding to the transformation $(\Lambda, S, h, \Sigma) \leftrightarrow (-\Lambda, -S, -h, \Sigma)$.

As $\Sigma \to \infty$, the function $\tanh(2\xi/\Sigma(1+h))$ tends to $2\xi/\Sigma(1+h)$. Consequently, the large Σ sinuous dispersion relation (2.20) reduces to

$$D = \frac{2\xi(1+S)(1/\Lambda + 1 - \omega/k)^2}{\Sigma(1+h)} + \frac{2\xi(1-S)(1/\Lambda - 1 - \omega/k)^2}{3\Sigma(1-h)}$$
$$+ \frac{\Sigma(1-h)(1-S)(1/\Lambda - 1 - \omega/k)^2}{2\xi} - \xi = 0. \quad (6.8)$$

In this limit the sinuous case still does not have any symmetries. This lack of symmetry offers no easy reformulation to help simplify the dispersion relation and even though analytic solutions can be derived, they are not informative. The large Σ sinuous instability is best understood by interpreting the dispersion relation physically. The pressure term in the inner flow is in general an $O(\Sigma^2)$ smaller than the pressure term in the outer flow. It is not sufficiently large to overcome surface tension or compete with the outer pressure in order to sustain oscillations at the interface. It is possible to balance the pressures at the required $O(\Sigma)$, but only in the neighbourhood of $0 < 1 + h < \Sigma^{-2}$. As Σ is increased above 1, therefore, the regions of absolute instability quickly become confined to a small sliver around $h = -1$ (figure 8).

6.2. *General surface tension*

The image system for varicose and sinuous perturbations at weak, normal and strong confinement is shown in figure 9. In the varicose case, the dimensional parameter set $(U_1, U_2, \rho_1, \rho_2, h_1, h_2, \sigma)$ is equivalent to $(U_2, U_1, \rho_2, \rho_1, h_2, h_1, \sigma)$. In non-dimensional terms, this is equivalent to the transformation $(\Lambda, S, h, \Sigma) \leftrightarrow (-\Lambda, -S, -h, \Sigma)$. Similarly, the sinuous case with (Λ, S, h, Σ) and strong confinement $(h \sim -1)$ also tends to the varicose case with $(-\Lambda, -S, -h, \Sigma)$. This is because the $\coth(2k/(1 + h)\Sigma)$ term in the varicose dispersion relation and the $\tanh(2k/(1 + h)\Sigma)$ term in

the sinuous are both approximately 1 when their arguments are large. Hence the symmetry $(\sin, \Lambda, S, h, \Sigma) \leftrightarrow (\text{var}, -\Lambda, -S, -h, \Sigma)$ can be expected to hold while $(16/9)M^2/(1 + h)\Sigma \gg 1$, which upon rearranging gives $1 + h \ll (16/9)(1/\Lambda + S)^2/\Sigma$. This restriction confines the varicose–sinuous symmetry to a region around $h = -1$, the size of which decreases as Σ increases.

Using these symmetries, regions of absolute instability in the strongly confined limit ($h = -1$) for both varicose and sinuous perturbations may be calculated from the unconfined ($h = 1$) varicose results under the transformation $(\Lambda, S) \leftrightarrow (-\Lambda, -S)$.

Figures 7 and 8 show regions of absolute instability as a function of confinement h and shear Λ, at various density measures S and over a range of surface tensions Σ, for varicose and sinuous perturbations respectively.

In the unconfined varicose case (figure 7a), regions of absolute instability move to lower density measures ($S < 0$) as Σ increases. In the confined varicose case, for the special case of $S = 0$, regions of absolute instability obey the symmetry $(\Lambda, h) \leftrightarrow (-\Lambda, -h)$, which can be inferred from (2.6). The most important points, however, are that, for $h > 0$, absolutely unstable regions are widest when $S < 0$ and that, for $h < 0$, absolutely unstable regions are widest when $S > 0$. This becomes increasingly prominent as the surface tension increases.

In the unconfined sinuous case (figure 8a), regions of absolute instability move to higher density measures ($S > 0$) and eventually disappear as Σ increases. In the confined sinuous case there are no longer any symmetries. The most important point is that, for weak confinement ($h > 0$), surface tension reduces absolute instability quite effectively but that, for strong confinement ($h < 0$), absolutely unstable regions persist with significant coflow, particularly for confined dense wakes.

7. Conclusions

This work has examined the effect of surface tension on the convective/absolute transition of confined and unconfined planar jets and wakes. Two different methods were used. The first was a spatio-temporal analysis, which follows modes with zero group velocity to determine convective/absolute transition boundaries over a range of different parameters. The second was a full impulse response method, which produces plots of the full impulse response at a given set of parameter values. Two modes govern the flows' behaviour: one in which the shear layers act independently, called the surface tension mode, and one in which the shear layers act in tandem, called the jet/wake column mode. The surface tension mode dominates the response at the front and back of the wavepacket and the jet/wake mode grows fastest in the cross-stream direction at the centre of the wavepacket (figure 3).

A single shear layer with surface tension was examined first because this provides information on the shear layer mode without the possibility of interaction with the jet/wake column mode. In $(1/\Lambda, S)$-space, the absolutely unstable region is an ellipse that extends into significant regions of coflow. This differs from a single shear layer without surface tension, which is absolutely unstable only in counterflow. The shear layer with surface tension is most absolutely unstable when the density measure $S \equiv (\rho_1 - \rho_2)/(\rho_1 + \rho_2)$ is equal to $1/2$, with the denser fluid moving more slowly than the less dense fluid.

For unconfined jets and wakes, the surface tension mode does not interact significantly with the primary jet/wake column mode when $\Sigma < 8M^2/9$, where M is the net mass flux, defined in §4.1. At these low values of Σ, the surface tension mode (light grey region in figure 4) is always more unstable than the jet/wake

column mode (dark grey region). When $\Sigma > 8M^2/9$, the surface tension mode and the jet/wake column modes start to interact. Increasing the surface tension causes varicose perturbations to be more unstable at $S < 0$ (light inner fluid) and more stable at $S > 0$ (dense inner fluid). The reverse is true for sinuous perturbations. At moderate values of Σ, therefore, jets and wakes with surface tension are more unstable than equivalent single shear layers with surface tension and much more unstable than equivalent jets and wakes without surface tension. Nevertheless, increasing Σ ultimately stabilizes all perturbations, whether sinuous or varicose.

For confined jets and wakes with $\Sigma \gg 1$, the behaviour of varicose perturbations, which are usually more unstable than sinuous perturbations, is symmetric under the transformation $(S, h) \leftrightarrow (h, S)$. In other words, the confinement behaves as if it changes the density ratio between the fluids. This leads to the fact that, for uniform density flows, the absolutely unstable region is an ellipse in $(1/\Lambda, h)$-space, which extends to $1/\Lambda = \pm 3$. For other density ratios, the flow is absolutely unstable when $8J' > 9M'^2$, where J' and M' are defined in §6.1. At high Σ, the varicose mode is very unstable, particularly for weakly confined light jets/wakes ($h > 0$, $S < 0$) and strongly confined dense jets/wakes ($h < 0$, $S > 0$).

For confined jets and wakes with $\Sigma \sim 1$, the concept of apparent density can be introduced. Confining the outer flow increases its apparent density. There are no further simplifications to be made, however, and the absolutely unstable regions must be read from figures 7 and 8. As for high surface tension, the varicose mode is particularly unstable for weakly confined light jets/wakes ($h > 0$, $S < 0$) and strongly confined dense jets/wakes ($h < 0$, $S > 0$). The sinuous mode is also unstable, particularly for confined dense wakes.

This work has revealed that surface tension considerably alters the stability of planar jets and wakes, whether unconfined or confined. While applying the results, however, it is important to bear in mind that they were derived for plug flow velocity profiles and inviscid fluids. The results will be inaccurate for $Re < 10^2$ but accurate for $Re > 10^3$. Similarly, they will not be applicable when the actual shear layer thickness exceeds the wavelength of the surface tension mode that is predicted by this model, $\lambda \sim \pi \sigma / (\rho_{ref} U_{ref}^2)$. Nevertheless, the results show that surface tension will have an appreciable effect on a laboratory experiment that has been designed by this group, for which Σ is in the range 0.25–25.

REFERENCES

Briggs, R. 1964 *Electron-Stream Interaction with Plasmas*. MIT Press.

Chen, J.-H., Pritchard, W. G. & Tavener, S. J. 1995 Bifurcation for flow past a cylinder between parallel planes. *J. Fluid Mech.* **284**, 23–41.

Davis, R. W., Moore, E. F & Purtell, L. P. 1983 A numerical-experimental study of confined flow around rectangular cylinders. *Phys. Fluids* **27** (1), 46–59.

De, A. K. & Dalal, A. 2007 Numerical study of laminar forced convection fluid flow and heat transfer from a triangular cylinder placed in a channel. *J. Heat Transfer* **129**, 646–656.

Drazin, P. G. & Reid, W. H. 1981 *Hydrodynamic Stability*. Cambridge University Press.

Esch, R. E. 1957 The instability of a shear layer between two parallel streams. *J. Fluid Mech.* **3**, 289–303.

Healey, J. J. 2006 A new convective instability of the rotating-disk boundary layer with growth normal to the disk. *J. Fluid Mech.* **560**, 279–310.

Healey, J. J. 2007 Enhancing the absolute instability of a boundary layer by adding a far-away plate. *J. Fluid Mech.* **579**, 29–61.

HUERRE, P. 2000 Open shear flow instabilities. In *Perspectives in Fluid Dynamics: A Collective Introduction to Current Research* (eds. G. K. Batchelor, H. K. Moffat & M. G. Worster). Cambridge University Press.

JENDOUBI, S. & STRYKOWSKI, P. J. 1994 Absolute and convective instability of axisymmetric jets with external flow. *Phys. Fluids* **6** (9), 3000–3009.

JUNIPER, M. P. 2006 The effect of confinement on the stability of two-dimensional shear flows. *J. Fluid Mech.* **565**, 171–195.

JUNIPER, M. P. 2007 The full impulse response of two-dimensional jet/wake flows and implications for confinement. *J. Fluid Mech.* **590**, 163–185.

JUNIPER, M. P. 2008 The effect of confinement on the stability of non-swirling round jet/wake flows. *J. Fluid Mech.* **605**, 227–252.

JUNIPER, M. P. & CANDEL, S. 2003 The stability of ducted compound flows and the consequences for the geometry of coaxial injectors. *J. Fluid Mech.* **482**, 257–269.

KIM, D.-H., YANG, K.-S. & SENDA, M. 2004 Large eddy simulation of turbulent flow past a square cylinder confined in a channel. *Comput. Fluids* **33**, 81–96.

LESSHAFFT, L. & HUERRE, P. 2007 Linear impulse response in hot round jets. *Phys. Fluids* **19**, 024102.

MELIGA, P., SIPP, D. & CHOMAZ, J.-M. 2008 Absolute instability in axisymmetric wakes: compressible and density variation effects. *J. Fluid Mech.* **600**, 373–401.

MONKEWITZ, P. 1988 The absolute and convective nature of instability in two-dimensional wakes at low Reynolds numbers. *Phys. Fluids* **31**, 999–1006.

RAYLEIGH, J. W. S. 1894 *The Theory of Sound*, vol. II. Dover.

REES, S. J. & JUNIPER, M. P. In press The effect of confinement on the stability of viscous planar jets and wakes. *J. Fluid Mech.*

RICHTER, A. & NAUDASCHER, E. 1976 Fluctuating forces on a rigid circular cylinder in confined flow. *J. Fluid Mech.* **78**, 561–576.

SHAIR, F., GROVE, A., PETERSEN, E. & ACRIVOS, A. 1963 The effect of confining walls on the stability of the steady wake behind a circular cylinder. *J. Fluid Mech.* **17**, 546–550.

SREENIVASAN, K. R., RAGHU, S. & KYLE, D. 1989 Absolute instability in variable density round jets. *Exp. Fluids* **7**, 309–317.

TURKI, S., ABBASI, H. & NASRALLAH, S. B. 2003 Effect of the blockage ratio on the flow in a channel with a built-in square cylinder. *Computation. Mech.* **33**, 22–29.

YU, M.-H. & MONKEWITZ, P. A. 1990 The effect of non-uniform density on the absolute instability of planar inertial jets and wakes. *Phys. Fluids* A **2** (7), 1175–1181.

YU, M.-H. & MONKEWITZ, P. A. 1993 Oscillations in the near field of a heated two-dimensional jet *J. Fluid Mech.* **255**, 323–347.